JGR Oceans

RESEARCH ARTICLE
10.1029/2025JC022518

Improved Theoretical Estimates of the Zonal Propagation of Global Nonlinear Mesoscale Eddies

Ran Liu[1,2], **Yan Wang**[1,2], **Xiaoming Zhai**[3], **Dhruv Balwada**[4], **and Julian Mak**[1,2,5]

[1]Department of Ocean Science, The Hong Kong University of Science and Technology, Hong Kong, China, [2]Center for Ocean Research in Hong Kong and Macau, The Hong Kong University of Science and Technology, Hong Kong, China, [3]School of Environmental Sciences, University of East Anglia, Norwich, UK, [4]Lamont-Doherty Earth Observatory, Columbia University, Palisades, NY, USA, [5]National Oceanography Centre, Southampton, UK

Key Points:

- Mesoscale eddy propagation speeds are accurately estimated by theoretical phase speeds of baroclinic Rossby waves incorporating eddy length scales
- Mesoscale eddy radii from satellite altimetry record can be readily used to estimate local eddy length scales

Correspondence to:
Y. Wang,
yanwang@ust.hk

Citation:
Liu, R., Wang, Y., Zhai, X., Balwada, D., & Mak, J. (2025). Improved theoretical estimates of the zonal propagation of global nonlinear mesoscale eddies. *Journal of Geophysical Research: Oceans*, *130*, e2025JC022518. https://doi.org/10.1029/2025JC022518

Received 20 FEB 2025
Accepted 5 JUN 2025

Author Contributions:

Conceptualization: Ran Liu
Data curation: Ran Liu
Formal analysis: Ran Liu
Funding acquisition: Yan Wang
Investigation: Ran Liu
Methodology: Ran Liu, Yan Wang, Xiaoming Zhai
Project administration: Yan Wang
Resources: Ran Liu
Software: Ran Liu
Supervision: Yan Wang
Validation: Ran Liu
Visualization: Ran Liu
Writing – original draft: Ran Liu
Writing – review & editing: Ran Liu, Yan Wang, Xiaoming Zhai, Dhruv Balwada, Julian Mak

Abstract Mesoscale eddies are essential for transport and mixing processes in the global ocean, with their characteristic westward propagation being a significant finding from the satellite altimetry era. Traditional predictions of their zonal propagation rely on the theoretical phase speed of long baroclinic Rossby waves; however, this approach is known to overestimate eddy speeds equatorward of approximately 35° latitudes. To address this issue, we incorporate local eddy wavelengths inferred from satellite-based eddy radii into the estimation of global eddy speeds, thereby significantly reducing the overestimation biases in mid-to low-latitude regions. This improvement is consistent with the observation that mesoscale eddies in these latitudes have length scales comparable to the local deformation scales and thus refrain from satisfying the long-wave approximation, whereas the long baroclinic Rossby wave phase speed remains useful for capturing the most energetic but less abundant eddies. The remaining discrepancies between the revised theoretical speeds and observations primarily stem from uncertainties in the background zonal flow, spatial variability of vertical modal structures (and the associated deformation radii), and estimation of local eddy length scales. These findings have important implications for understanding long-range mesoscale eddy propagation and eddy-driven mixing in the global ocean, which are anticipated to benefit future ocean model developments and enhance predictions of mesoscale eddy dynamics.

Plain Language Summary Mesoscale eddies are crucial features in the ocean that facilitate the transport and mixing of water masses, significantly influencing ocean dynamics. One of their defining traits is their tendency to move westward, a phenomenon made more evident with satellite altimetry technology. Traditional predictions of the east-to-west traveling speeds of these eddies rely on a theory of long planetary ocean waves. However, this approach often overestimates eddy speeds, particularly for those in the tropics. This study addresses this issue by utilizing satellite data to determine the local wavelengths of these eddies, enabling more accurate predictions of their movements. Our findings suggest that the size of mesoscale eddies can effectively be used to estimate their local wavelengths. It is noteworthy that the long planetary wave speed remains useful for estimating the speeds of the most energetic but less common eddies. These insights are important for enhancing our understanding of how mesoscale eddies propagate over long distances and their role in ocean mixing. Ultimately, this research will contribute to ocean model developments and enhance our ability to predict the behaviors of ocean eddies.

1. Introduction

Mesoscale eddies are ubiquitous and dynamically important features in the world's oceans (Chelton et al., 2011). These coherent structures typically span 10–100 km in the horizontal and survive for several weeks to over a year (Abernathey & Haller, 2018; Chelton et al., 2011; Wortham & Wunsch, 2014; Wunsch & Stammer, 1995). By redistributing heat (Wang et al., 2023), nutrients (Uchida et al., 2020), chlorophyll (McGillicuddy, 2016), dissolved greenhouse gases (Youngs et al., 2023), and other oceanic tracers (Atkins et al., 2022), and transferring momentum and energy across multiple spatial scales of oceanic processes (Balwada et al., 2022; Capet et al., 2008; McWilliams, 2008; Salmon, 1982; Scott & Wang, 2005), these eddies profoundly impact the global ocean circulation, biogeochemistry, long-term climate evolution, and even extreme events (Atkins et al., 2022; Bian et al., 2023; He et al., 2023; McGillicuddy, 2016).

The aggregation of satellite altimetry records over the past few decades has enabled a long-range, global-scale census of mesoscale eddies by tracking anomalous sea surface height (SSH) signatures (Chelton et al., 2011);

such a census has provided valuable insights into the distributions, kinematic features, and potential impacts of mesoscale eddies. Among various statistical characteristics of mesoscale eddies, the eddy zonal propagation or translation speed can be accurately estimated via classical geostrophic turbulence theories. Specifically, the theoretical zonal phase speed of long baroclinic Rossby waves has routinely been employed to interpret the predominantly westward propagation behavior of mesoscale eddies (Chelton et al., 2007; Cushman-Roisin et al., 1990; Killworth, 1986; McWilliams & Flierl, 1979; Xu & Oey, 2015) and to inform closure theories of eddy-driven mixing processes in the global ocean (Abernathey & Wortham, 2015; Ferrari & Nikurashin, 2010; Klocker & Abernathey, 2014; Klocker et al., 2016).

Early studies have shown that the theoretical zonal phase speed of long baroclinic Rossby waves roughly matches the phase speed of planetary-scale SSH signatures in Hovmöller diagrams equatorward of $\sim 20°$ latitudes; these SSH signatures have since been interpreted as the first mode of baroclinic Rossby waves (Chelton & Schlax, 1996). However, the speeds of these observed wave signatures tend to be underestimated by theory in mid-to high-latitudes (Chelton et al., 2007, 2011; Chelton & Schlax, 1996). Lots of efforts have been made to diminish the deviations between the theory and observation by retrieving the effects that were neglected in the classical linear wave theory, such as topography, background flow, bottom friction and so on (Aoki et al., 2009; Tailleux, 2012; Tailleux & McWilliams, 2000, 2001). Recent studies addressed this underestimation issue by accounting for the local background flow conditions and finite wavelengths (Tulloch et al., 2009), and by revising the calculation of local deformation radii over a rough seafloor (Lacasce, 2017; LaCasce & Groeskamp, 2020). On the other hand, when the theoretical zonal phase speed of long baroclinic Rossby waves was applied for quantifying mesoscale eddy propagation documented in the altimetry-based eddy census, it was found to substantially overestimate westward eddy propagation speeds equatorward of $\sim 35°$ latitudes (Chelton et al., 2007, 2011), even if the Doppler shift of eddy propagation induced by the depth-mean zonal flow velocity was taken into account (Abernathey & Wortham, 2015; Klocker & Abernathey, 2014; Klocker & Marshall, 2014). Moreover, the zonal propagation speeds documented by the altimetry-based eddy census generally differ from those of SSH signatures inferred from Hovmöller diagrams (Chelton et al., 2007), which results in varied utilities of the long-wave approximation in quantifying wave or eddy movements at different geographic locations.

Despite the apparent disparity between the theoretical long-wave zonal phase speeds and the observed eddy zonal propagation speeds across mid- to low-latitudes, existing studies of mesoscale eddy mixing, including those focusing on global-scale eddy diffusivity quantification (Groeskamp et al., 2020; Klocker & Abernathey, 2014), parameterization of eddy mixing (Ferrari & Nikurashin, 2010), and climate response to eddy mixing (Busecke & Abernathey, 2019), routinely employ the theoretical long-wave zonal phase speeds to characterize eddy zonal propagation, which, in turn, informs the strength and spatial pattern of eddy mixing (Ferrari & Nikurashin, 2010; Kong & Jansen, 2017). Such an approach leads to significant biases in the predicted strength of eddy mixing, particularly across mid-to low-latitudes (Klocker & Abernathey, 2014).

Given these long-standing issues in characterizing mesoscale eddy propagation and estimating global-scale eddy mixing, two fundamental questions arise. First, can additional factors be incorporated into existing theories to enable accurate and universal estimates of mesoscale eddy zonal propagation speeds globally? Second, why do observed zonal eddy propagation speeds documented in the altimetry-based census (Chelton et al., 2011) deviate from zonal phase speeds of SSH in Hovmöller diagrams or wavenumer-frequency spectral analyses, particularly at low latitudes where waves and eddies are readily overlapped in spectral space (Tulloch et al., 2009)?

This study addresses both questions by relaxing the widely used long-wave approximation and by invoking a broad range of length scales of mesoscale turbulence. We evaluate theoretical baroclinic Rossby wave phase speeds, incorporating local eddy length scales, against observed mesoscale eddy propagation speeds globally. Our results show substantially improved accuracy across most latitudes compared to existing theoretical predictions. This enhanced accuracy stems from the adaptability of the revised theory to abundant mesoscale eddies with horizontal scales comparable to local deformation radii. Furthermore, our new estimation elucidates the fundamental difference between the most energetic eddies or energy-containing eddies (Kong & Jansen, 2017) detected by SSH Hovmöller diagrams and the majority of observed eddies across the global ocean.

2. Materials and Methods

2.1. Observational Mesoscale Eddy Zonal Propagation Speed

In this study, the observational zonal propagation speed, denoted by C_{obs}, of each eddy on each day is determined by calculating the corresponding zonal displacement along the eddy trajectory one day before and after that day, and then dividing this displacement by the time span of 2 days. The altimetric mesoscale eddy trajectory atlas was produced by SSALTO/DUACS and distributed by AVISO+ (Pegliasco et al., 2022). Only eddy trajectories corresponding to the mature eddy phases are analyzed, selected by excluding the first and final 10% of each trajectory associated with the eddy genesis and demise phases (Z. Zhang & Qiu, 2018). Next, the geographic location of each eddy, covered by all selected eddy trajectories, is treated as the initial location of a new eddy pathway segment, which resembles a "pseudo-trajectory" defined in previous studies (Klocker et al., 2012; Chen & Waterman, 2017; W. Zhang & Wolfe, 2024). All pertinent eddy properties, including eddy radius, zonal eddy phase speed, geographic and temporal coordinates, are averaged from the date of any initial location of the eddy segment for 21 consecutive days and then recorded for that eddy segment. Adjusting the temporal length of the eddy segment primarily influences the sample size, but not the main conclusions drawn from this article. In general, this eddy segment processing approach carries two major advantages:

1. It substantially increases the sample size to enhance statistical robustness under various filtering conditions; a total of 805,894 (854,855) anticyclonic (cyclonic) eddy trajectories yield 1,696,845 (1,803,046) eddy segments globally.
2. The eddy properties at each spatial and temporal location can be more accurately quantified via averages across short-term eddy segments, as opposed to full eddy lifecycles, given that a mesoscale eddy can persist across different seasons and propagate for very long distances.

To interpret and compare with the results of Tulloch et al. (2009), we further employ the Radon transform estimation of SSH anomaly propagation speeds C_{Radon}, constructed by C. W. Hughes (personal communication). This global data set also builds upon the quarter-degree AVISO gridded sea level data. Weekly estimates are made to determine the zonal propagation speeds of SSH anomalies per 5-longitudinal-degree overlapping patch centered on each quarter-degree grid point (each patch thus covers 21 longitudinal grid points). The most updated data set covers SSH records from 1993 to December 14th, 2016. For applying the Radon transform, filtering was adopted to retain SSH signatures with periods between 21 and 168 days. In this work, we interpolate C_{Radon} onto each eddy position to make as fair a comparison as possible against various definitions of eddy phase speed.

2.2. Barotropic Zonal Velocity of Background Flow

The observational barotropic zonal velocity (or more precisely, the depth-mean velocity) of the background flow is estimated by invoking the thermal wind relation and then depth-averaging, that is,

$$u_b = \frac{1}{H}\int_{-H}^{0} u_g \, dz, \qquad \frac{\partial u_g}{\partial z} = \frac{g}{\rho_0 f}\frac{\partial \rho}{\partial y}, \tag{1}$$

where u_g denotes the background geostrophic zonal velocity, H measures the local ocean depth, $\rho_0 = 1000\,\mathrm{kg/m^3}$ represents a constant reference density, f stands for the local Coriolis frequency, and ρ is the potential density. To exploit the thermal wind relation, a reference depth is defined at the seafloor, where the zonal velocity is assumed to vanish. The potential density ρ is calculated through the TEOS-10 toolbox (McDougall & Barker, 2011), for which the required full-depth temperature and salinity are obtained from Met Office Hadley Center observational data set (version number EN.4.2.2.c14) with a regular 1-degree latitude/longitude grid resolution (Cheng et al., 2014; Good et al., 2013). Since mesoscale eddy trajectories cover the years 1993–2021, the corresponding monthly u_b is calculated also from 1993 to 2021. Consistent with the calculation of u_g, the meridional background velocity v_g is estimated following identical procedures and adopted for extracting the linear quasi-geostrophic (QG) wave solutions, detailed below.

2.3. Deformation Radii

The first baroclinic Rossby deformation radius is estimated as

$$L_d = \frac{\int_{-H}^{0} N dz}{\pi |f|} \tag{2}$$

across most latitudes and is approximated as

$$L_d = \left(\frac{\int_{-H}^{0} N dz}{2\pi\beta} \right)^{1/2} \tag{3}$$

in tropical regions within 5 latitudinal degrees from (but excluding) the equator (Chelton et al., 1998). Here, N denotes the buoyancy frequency, and β is the planetary vorticity gradient. We use the monthly climatology density field of EN.4.2.2.c14 data to calculate L_d following Equations 2 and 3 through years 1993−2021, and then interpolate the calculated L_d onto all eddy segments of the corresponding months and years. Following Tulloch et al. (2011), we further define the deformation wavelength as $L_{Rd} = 2\pi L_d$.

The deformation radius L_d defined following Equations 2 and 3 presumes a flat seafloor. To complement our analyses, we further consider the surface mode deformation radius, $L_d|_{\text{surf}}$, in place of L_d wherever possible when estimating the eddy phase speed. The global estimation of $L_d|_{\text{surf}}$ by LaCasce and Groeskamp (2020) based on the World Ocean Atlas 2018 climatology data set (Garcia et al., 2019) alongside a rough seafloor condition (i.e., by assuming vanishing geostrophic velocity at the ocean bottom) is utilized throughout this work.

2.4. Theoretical Zonal Eddy Phase Speeds

Following Klocker and Marshall (2014), we assume that the barotropic component of zonal mean flow imposes a Doppler-shift effect on the eddy zonal propagation, but neglect any advective impact from the mean baroclinic flow. As stressed in Klocker and Marshall (2014), this latter impact on nonlinear eddy propagation remains to be well constrained theoretically. Thus, the theoretical zonal eddy phase speed has been constantly quantified using the zonal phase speed of long baroclinic Rossby waves, Doppler-shifted by u_b (Groeskamp et al., 2020; Klocker & Marshall, 2014), that is,

$$C_{lw} = u_b - \beta L_d^2 \tag{4}$$

over a flat seafloor and

$$C_{lw}|_{\text{surf}} = u_b - \beta L_d|_{\text{surf}}^2 \tag{5}$$

over a rough sea floor.

Considering that mesoscale eddies do not necessarily satisfy the long wave approximation at all latitudes, a revised theoretical zonal eddy phase speed is proposed,

$$C_{e,L_d} = u_b - \frac{\beta}{K^2 + L_d^{-2}}, \tag{6}$$

where $K^2 = K_x^2 + K_y^2$ represents the squared horizontal eddy wavenumber with $[K_x,\ K_y]$ indicating the zonal and meridional wavenumber components. Assuming mesoscale eddies to be horizontally isotropic, one obtains:

$$K^2 = 2\left(\frac{2\pi}{\alpha L_e}\right)^2. \tag{7}$$

Here, $L_e = 4R$ stands for the eddy length scale, assumed to be greater than the eddy radius R by a factor of four (Tulloch et al., 2011), and α is an empirically determined correction factor, set to unity by default; the uncertainties associated with α are discussed in §4. This correction factor remedies the deviation of R, which was empirically defined as the radius of a circle with an identical area to that of the SSH contour associated with the maximized circum-average geostrophic speed of an eddy (Chelton et al., 2011), from one-fourth the eddy length

scale. It also accounts for the skewed distribution of statistical characteristics of eddy radii caused by the blind zone of satellite altimetry resolution (Figures 1c and 1d) and estimation errors introduced by eddy horizontal anisotropy (Stewart et al., 2015). An alternative form of the revised theoretical zonal eddy phase speed, using the surface deformation radius $L_d|_{\mathrm{surf}}$ in place of L_d in Equation 6, is analogously tested and denoted by $C_{e,L_d|_{\mathrm{surf}}}$ throughout this paper.

2.5. Linear Wave Phase Speed

In this study, we quantify the linear wave phase speeds based on the linearized QG potential vorticity (PV) equation, which, upon taking a wave form solution, yields an eigenvalue problem (Smith, 2007; Tulloch et al., 2009):

$$\begin{aligned}
(K_x u_g + K_y v_g - \omega_n)\,\hat{q}_n &= \left(K_y \frac{\partial \mathcal{Q}}{\partial x} - K_x \frac{\partial \mathcal{Q}}{\partial y}\right)\hat{\psi}_n, \quad -\mathrm{H} < \mathrm{z} < 0, \\
(K_x u_g + K_y v_g - \omega_n)\,\hat{b}_n &= \left(K_y \frac{\partial \mathcal{B}}{\partial x} - K_x \frac{\partial \mathcal{B}}{\partial y}\right)\hat{\psi}_n, \quad \mathrm{z} = 0, \\
(K_x u_g + K_y v_g - \omega_n)\,\hat{b}_n &= \left[K_y\left(\frac{\partial \mathcal{B}}{\partial x} - N^2\frac{\partial H}{\partial x}\right) - K_x\left(\frac{\partial \mathcal{B}}{\partial y} - N^2\frac{\partial H}{\partial y}\right)\right]\hat{\psi}_n, \quad \mathrm{z} = -\mathrm{H}.
\end{aligned} \tag{8}$$

Here, $\hat{\bullet}_n$ represents the wave amplitude of the nth Fourier mode, q is the eddy PV, b stands for the eddy buoyancy anomaly, ψ denotes the eddy geostrophic streamfunction, and the mean buoyancy and PV gradients are related to the background geostrophic velocity through $\nabla\mathcal{B} = \left[f\frac{\partial v_g}{\partial z}, -f\frac{\partial u_g}{\partial z}\right]$ and $\nabla\mathcal{Q} = \left[\frac{\partial}{\partial z}\left(\frac{f^2}{N^2}\frac{\partial v_g}{\partial z}\right),\ \beta - \frac{\partial}{\partial z}\left(\frac{f^2}{N^2}\frac{\partial u_g}{\partial z}\right)\right]$, respectively. The eigenvalue ω_n corresponds to the complex frequency of a wave solution; the real part of ω_n governs the phase propagation and the imaginary part, if any, represents the growth or decay rate of the wave. To implement the eigenvalue solver, we again utilize the three-dimensional climatological thermal wind velocity and stratification calculated from EN.4.2.2.c14 in each 1° × 1° grid box across the globe. Details of implementing this eigenvalue solver are given by Smith (2007).

To extract the zonal phase speeds of linear waves, $C = \frac{\mathbb{R}\{\omega_n\}}{K_x}$, we have retained our assumption of horizontal isotropy ($K_x = K_y$) to maintain consistency with other definitions of eddy phase speed. Tulloch et al. (2009) noted little difference between waves with horizontal isotropy and those with purely zonal phase propagation ($K_y = 0$) in seeking consistent wave solutions with the Radon transform of SSH anomalies. Two wavelength scales are analyzed in detail in this study. The first length scale, corresponding to those of the deformation-scale eddies and thus the short-wave limit, has $K_x = 1/L_d$ (Tulloch et al., 2009). Then at each geographic location, we follow Tulloch et al. (2009) to select the wave solution with a vertical structure (i.e., the real part of the eigenvector) projecting the most onto the first baroclinic mode, $\Phi_m|_{m=1}$, which corresponds to the first-mode solution of the Sturm-Liouville problem derived from the linearized QG system with no background flow nor bottom topography (Vallis, 2017):

$$\frac{d}{dz}\left(\frac{f^2}{N^2}\frac{d\Phi_m}{dz}\right) = -K_m^2\,\Phi_m, \qquad \left.\frac{d\Phi_m}{dz}\right|_{z=0,\ -H} = 0. \tag{9}$$

The corresponding linear wave phase speed is denoted as $C_{ProjBC1|_{\mathrm{L_d}}}$. We note in passing that the inverse of K_m yields a suite of deformation radii associated with an orthogonal family of neutral Rossby modes, yet the first baroclinic deformation radius calculated from the Sturm-Liouville problem is nearly identical to that formulated under the Wentzel–Kramers–Brillouin approximation in Equations 2 and 3 (Chelton et al., 1998). The second length scale is defined as the averaged observed mesoscale eddy radius over each 1° × 1° grid, hence with $K_x \simeq \frac{2\pi}{4R}$. In this case, projecting the linear wave solutions onto the first baroclinic modes results in a slower phase speed at lower latitudes compared to $C_{ProjBC1|_{\mathrm{L_d}}}$ and produces a highly discontinuous meridional profile of phase speeds at high latitudes, impeding meaningful analyses. Consequently, we opt for the locally fastest-growing unstable wave solution, whose phase speed is denoted as $C_{MaxGrowth|_{4R}}$. This choice echoes with existing analyses showing that the most unstable linear waves can control the kinematic properties of nonlinear mesoscale

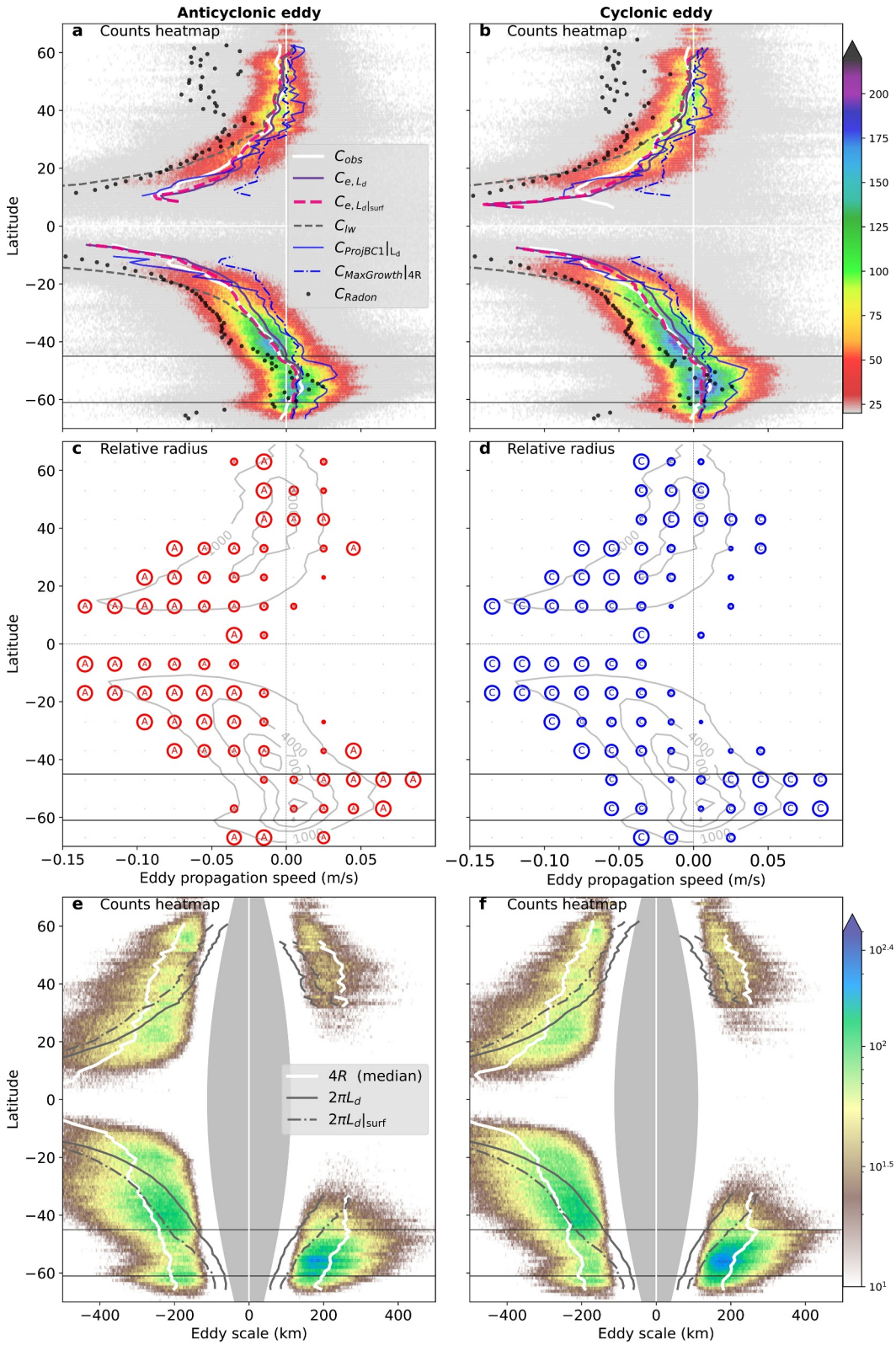

Figure 1.

eddies in spectral space (Berloff & Kamenkovich, 2013a, 2013b). In this study, this approach offers further insight into the complex dynamics underlying the propagation speeds of mesoscale eddies in physical space.

3. Results

3.1. Global Zonal Eddy Propagation Speeds

The preferred zonal propagation speeds of mesoscale eddies across the globe are shown as white curves in Figures 1a and 1b, quantified as the zonally averaged zonal speeds of anticyclonic eddies (AE) and cyclonic eddies (CE), respectively, per latitudinal-degree interval. It is noteworthy that the zonal average and the median of eddy propagation speeds within each latitudinal internal are nearly identical when both westward and eastward eddies are accounted for. Moreover, consistent with the eddy census of Chelton et al. (2011), the westward eddy propagation is systematically slower than the Radon transform estimation (black dots) nearly everywhere across the globe.

Equatorward of $\sim 35°$ latitudes, the long Rossby wave phase speeds (gray dashed curves), even accounting further for the Doppler-shifting by the background flow, still substantially deviate from the observed zonal propagation speeds of both AE and CE, which is consistent with previous findings (Chelton et al., 2007, 2011; Klocker & Abernathey, 2014; Klocker & Marshall, 2014). In contrast, the revised theoretical speed (magenta and purple curves), which incorporate local eddy length scales, show much better agreements with observations. It is worth noting that this improvement holds whether the deformation radius is based on the surface mode (over a rough seafloor) or the classical baroclinic mode (over a flat bottom). Between the two revised theoretical speed estimates, the surface mode deformation radius, $L_d|_{\mathrm{surf}}$, yields a closer alignment with observed propagation speeds in low- to mid-latitudes, whereas the flat bottom-based L_d yields a slight underestimation. In summary, incorporating local eddy length scales systematically reduces the overestimation from the classical long-wave theory, and any remaining discrepancy might has arisen from uncertainties in the background zonal velocity, deformation radius estimates, and local eddy scale quantification, which are further discussed later.

Since the pseudo-trajectory method facilitates accurate estimates of eddy propagation speeds for each month, it is intriguing to further investigate the seasonal variation of eddy propagation speeds, shown in Figure 2. The difference of preferred eddy zonal propagation speed between boreal winter and summer is very slight for both AE and CE. Moreover, the revised theoretical phase speed incorporating local eddy length scales still outperforms other theoretical estimates, regardless of the season considered.

The much improved alignment of the revised theoretical phase speeds with the observed eddy propagation speeds has two key implications, listed as follows.

First, mesoscale eddy propagation is dispersive; eddy sizes directly influence the propagation speeds. This is clear in Figures 1c and 1d: faster westward-propagating mesoscale eddies generally have larger radii within each latitudinal band, particularly equatorward of $\sim 35°$ latitudes. Eastward-propagating eddies, such as those in the Antarctic Circumpolar Current (ACC), exhibit similar dispersive behaviors. However, these dispersive features may depend intrinsically on the eastward background flow itself. Specifically, Liu et al. (2024) utilized a suite of idealized simulations to show that eddies in the ACC cascade toward larger scales if the background flow is faster.

Figure 1. (a) Heatmap of anticyclonic eddy counts as a function of eddy zonal propagation speed and latitude for years 1993–2021. White curves indicate zonally averaged zonal propagation eddy speeds (C_{obs}) per 1-degree latitude. Purple and magenta curves indicate theoretical baroclinic Rossby wave zonal phase speeds incorporating L_d (C_{e,L_d}) and $L_d|_{\mathrm{surf}}$ ($C_{e,L_d|_{\mathrm{surf}}}$), respectively, both accounting for the advection of depth-mean background zonal velocity and the local eddy length scale. Gray dashed curves indicate long baroclinic Rossby wave phase speeds with the Doppler-shift effect from the background zonal flow (C_{lw}). Black dots indicate zonal speeds of sea surface height anomalies inferred from Radon transform (C_{Radon}). Blue solid and dashed-dotted curves indicate the zonal speeds of linear quasi-geostrophic potential vorticity waves, whose wavelengths are respectively estimated with local deformation scales ($C_{ProjBC1}|_{\mathrm{Ld}}$) and with actual mesoscale eddy scales ($C_{MaxGrowth}|_{4\mathrm{R}}$). (b) Similar to (a) but for cyclonic eddies (CE). (c) The sizes of the red circles indicate the relative median of radii of anticyclonic eddies, quantified by grouping eddy radii into bins of 1 cm/s $\times$ 2° (in latitude) and then normalizing the medians of radii in each 2° latitudinal band. The background gray contours show the eddy counts in each bin. (d) Similar to (c) but for CE. (e) Heatmap of anticyclonic eddy counts as a function of eddy length scale and latitude for years 1993–2021. White curves show the fourfold-amplified median of anticyclonic radii ($4R$) per 1-degree latitude. Gray solid curves represent averaged first baroclinic deformation radii calculated for a flat-bottomed ocean ($2\pi L_d$) on all eddy locations, whereas dashed-dotted curves correspond to averaged surface mode radii ($2\pi L_d|_{\mathrm{surf}}$). Negative (positive) length scales correspond to westward-propagating (eastward-propagating) eddies. (f) Similar to (e) but for CE. Panels (a), (b), (c), and (d) use identical axes. Black horizontal lines delineate the Antarctic Circumpolar Current region. Gray shadings in (e) and (f) indicate blinded scales due to satellite altimeter resolution.

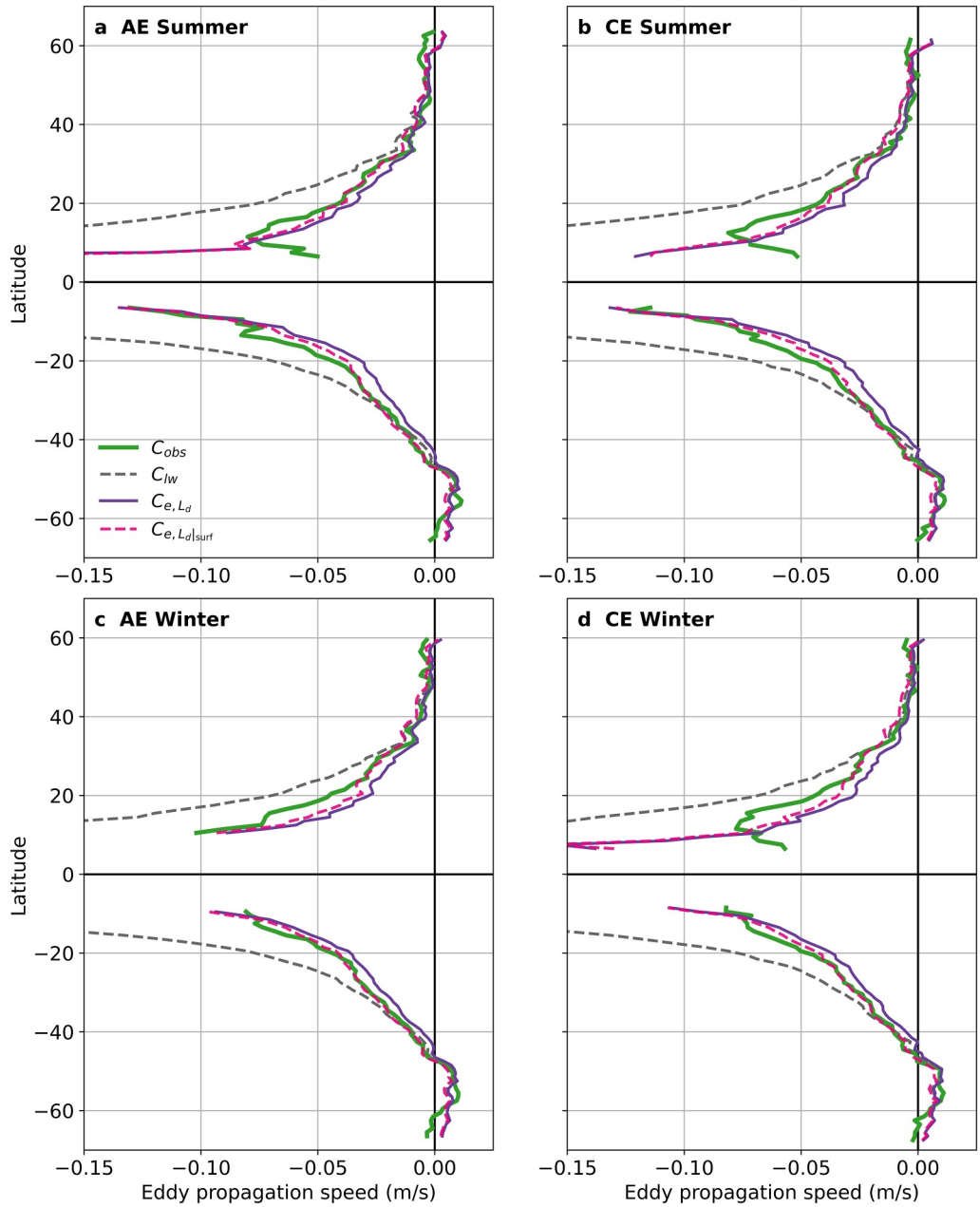

Figure 2. (a) Green curves indicate observed anticyclonic eddy (AE) zonal propagation speed per 1-degree latitudinal interval in boreal summer (averaged through June, July, and August). Purple and magenta curves indicate theoretical baroclinic Rossby wave zonal phase speeds calculated using L_d (C_{e,L_d}) and $L_d|_{\text{surf}}$ ($C_{e,L_d|_{\text{surf}}}$), respectively, both accounting for the advection of depth-mean background zonal velocity and the local eddy length scale. Gray dashed curves indicate long baroclinic Rossby wave phase speeds. (b) Similar to (a) but for cyclonic eddies (CE). (c) Similar to (a) but for the boreal winter season (averaged through December, January, and February). (d) Similar to (c) but for CE.

Second, eddies across 10°–35° latitudes cannot be accurately framed by the long-wave approximation. This is further illustrated in Figures 1e and 1f, which compare the local deformation radii (amplified by a factor of 2π) defined over either flat or rough bottoms (LaCasce & Groeskamp, 2020), against the observational eddy length scales, quantified as fourfold-amplified coherent eddy radii (Tulloch et al., 2011). The ratio of the eddy length scale to the deformation scale drops rapidly toward the equator. The crossovers between the two length scales occur at approximately 30°N (25°N) and 30°S (20°S) if one takes a rough (flat) seafloor into account.

To take the full background flow conditions (i.e., mean vertical shears and topographic PV gradients) into account, we further calculate the zonal propagation speeds of linear PV waves projecting mostly onto the local first baroclinic neutral modes following Tulloch et al. (2009), each of which integrates a selected wavelength of the local deformation scale (deformation scale waves hereafter). The zonal propagation of deformation scale waves conspicuously deviates from the Radon transform estimation (black dots) nearly everywhere globally, consistent with the findings of Tulloch et al. (2009) in the central Pacific. In parallel, the deformation scale wave speeds align closely with the revised theoretical phase speeds equatorward of approximately ∼20°, where the deformation wavelengths exceed the average observational eddy length scales. Toward higher latitudes, the deformation scale waves exhibit consistently slower westward propagation than observed eddies, particularly across the enhanced eastward background flow of the Southern Ocean. Other possible linear wave solutions, including the unstable modes with the locally fastest growth rates and observed eddy scales (blue dashed-dotted curves), are also examined. The speeds of the fastest growing modes with observed eddy scales can align with the observed eddy propagation speeds in the Southern Ocean, but greatly underestimate the eddy propagation in lower latitudes.

Overall, the revised theoretical phase speed proposed in this work offers a more accurate and convenient estimate of the observational mesoscale eddy propagation speed globally. In contrast, wave solutions extracted from the linearized QG system incorporating full background flow conditions and finite wavelengths are less accurate in estimating the observed global eddy propagation.

3.2. Parameter Regimes of Theory-Observation Deviations of Eddy Propagation

To further quantify the efficacy of the revised theory in estimating eddy propagation speeds across mid- to low-latitudes (within 35° from equator), we show in Figure 3 the relative errors (gray, white, and light green contours) of theoretical against observed zonal propagation speeds of all westward-propagating eddies globally (note from Figure 1 that eddy propagation is predominantly westward in low latitudes), superposed on the base-10 logarithms of eddy counts per unit horizontal area throughout the satellite altimetry era. A parameter regime diagram can then be constructed by plotting both quantities as functions of the normalized eddy length scale by the deformation wavelength (L_e/L_{Rd}) and the eddy nonlinearity, the latter of which is quantified as the ratio of eddy rotational to eddy propagation speeds (Chelton et al., 2011; Klocker et al., 2016). The thus constructed regime diagram highlights the parameter space across which long-wave and revised theories of eddy propagation are valid.

Figure 3 reveals that most westward-propagating eddies have normalized length scales below ∼1.2 and nonlinearity bounded by ∼2.5, regardless of the eddy polarity. These eddies, with relatively small length scales, are abundant but do not conform to the long-wave approximation. Consequently, using the long-wave approximation to estimate eddy propagation speeds results in relative errors readily beyond ±25% (indicated by regions beyond those enclosed by gray solid and dashed contours). Specifically, only 31.5% of AE and 33.0% of CE are associated with relative errors bounded by ±25% if the long-wave approximation is adopted.

In contrast, the revised theoretical framework, which incorporates local eddy length scales, accurately captures the movement of eddies that satisfy the long-wave approximation and, importantly, those with moderate nonlinearity and length scales comparable to the deformation scales; the latter batch of eddies mainly fall into the region termed Regime 3, enclosed by both the white and the light green contours in Figure 3. Geographically, these eddies are primarily found within 35° latitudes from equator (Figure 4c). This is consistent with the improved agreement between theoretical and observational eddy propagation speeds across low-to-mid latitudes shown in Figure 1. Quantitatively, under the revised framework, the fraction of propagation speed records with relative errors bounded by ±25% increases to 75.3% (74.2%) for AE and 69.0% (76.1%) for CE when L_d ($L_{d|_{\text{surf}}}$) is adopted.

Further analyses of the relative error differences resulting from adopting L_d versus $L_{d|_{\text{surf}}}$ in theory motivate us to delineate two additional regimes. Eddies falling into the Regime 2 highlighted in Figure 3 can be more sensitive to bottom roughness, since the calculated relative errors of theoretical propagation speeds are consistently smaller when $L_{d|_{\text{surf}}}$ is adopted. These eddies are predominantly located in the open ocean across 30°–50° latitudes, particularly in the North and South Pacific and in the North Atlantic (Figure 4b). In parallel, the zonal propagation

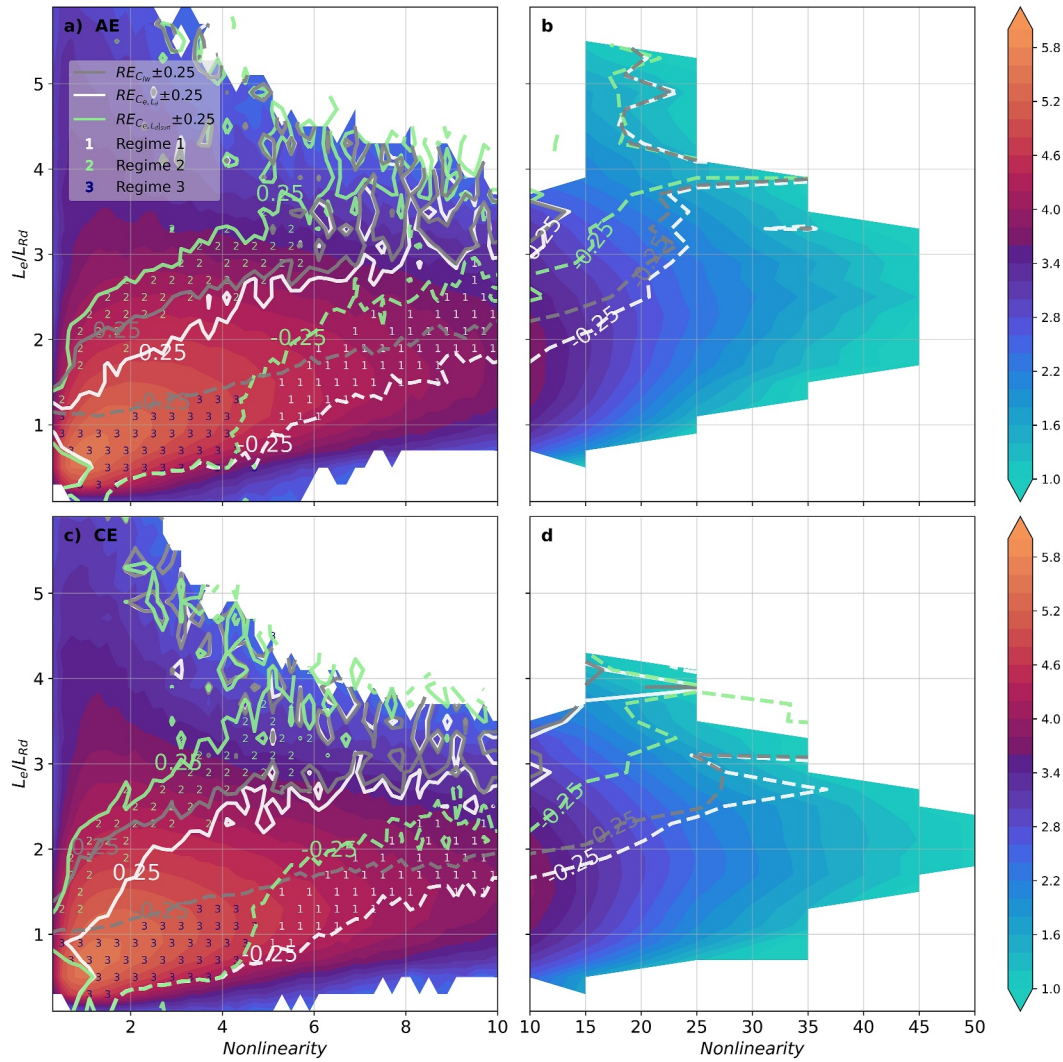

Figure 3. (a) The color shading represents the base-10 logarithm of the number of westward-propagating anticyclonic eddies per unit horizontal area during the satellite altimetry era, plotted against the eddy nonlinearity and normalized eddy length scale. Thick white and light green contours mark regions where the relative error (RE) between the observed eddy speeds and the revised theoretical eddy propagation speeds calculated using C_{e,L_d} and $C_{e,L_d|\mathrm{surf}}$, respectively, falls within ±25%. Gray contours, defined similarly, are constructed using the long baroclinic Rossby wave phase speed for theoretical estimation. Three regions are highlighted with numbers, which represent three eddy regimes. Regime 1 is delineated by $\mathrm{RE}|_{C_{lw}} < -0.25$ and $\mathrm{RE}|_{C_{e,L_d}} > -0.25$; Regime 2 is delineated by $\mathrm{RE}|_{C_{e,L_d|\mathrm{surf}}} < 0.25$ and $\mathrm{RE}|_{C_{e,L_d}} > 0.25$; Regime 3 is delineated by $\mathrm{RE}|_{C_{lw}} < -0.25$ and $\mathrm{RE}|_{C_{e,L_d|\mathrm{surf}}} > -0.25$. (b) Similar to (a) but for eddies with the nonlinearity parameter exceeding 10. (c) Similar to (a) but for cyclonic eddies. (d) Similar to (c) but for eddies with the nonlinearity parameter exceeding 10. Owing to uncertainties in estimating the depth-mean background velocity, only theoretically estimated eddy propagation speeds with a westward direction are considered for calculating the relative errors, covering over 85% of observed westward eddy propagation records.

of eddies in the vicinity of the eastern boundaries of major ocean basins around 35° latitudes is more appropriately framed by L_d (Figure 4a).

Eastward-propagating eddies are primarily observed in the Southern Ocean, influenced by the Doppler-shift effect of the ACC (Klocker & Marshall, 2014). Compared to westward-propagating eddies, eastward-propagating eddies generally have normalized length scales exceeding unity, largely due to the smaller deformation radii at high latitudes (Figure 1). Consequently, the revised theoretical propagation speed converges to the long-wave approximation phase speed, minimizing the difference between the long-wave approximation and the revised theories of eddy propagation speed (Figures 1 and 5). It is noteworthy that both theories can accurately

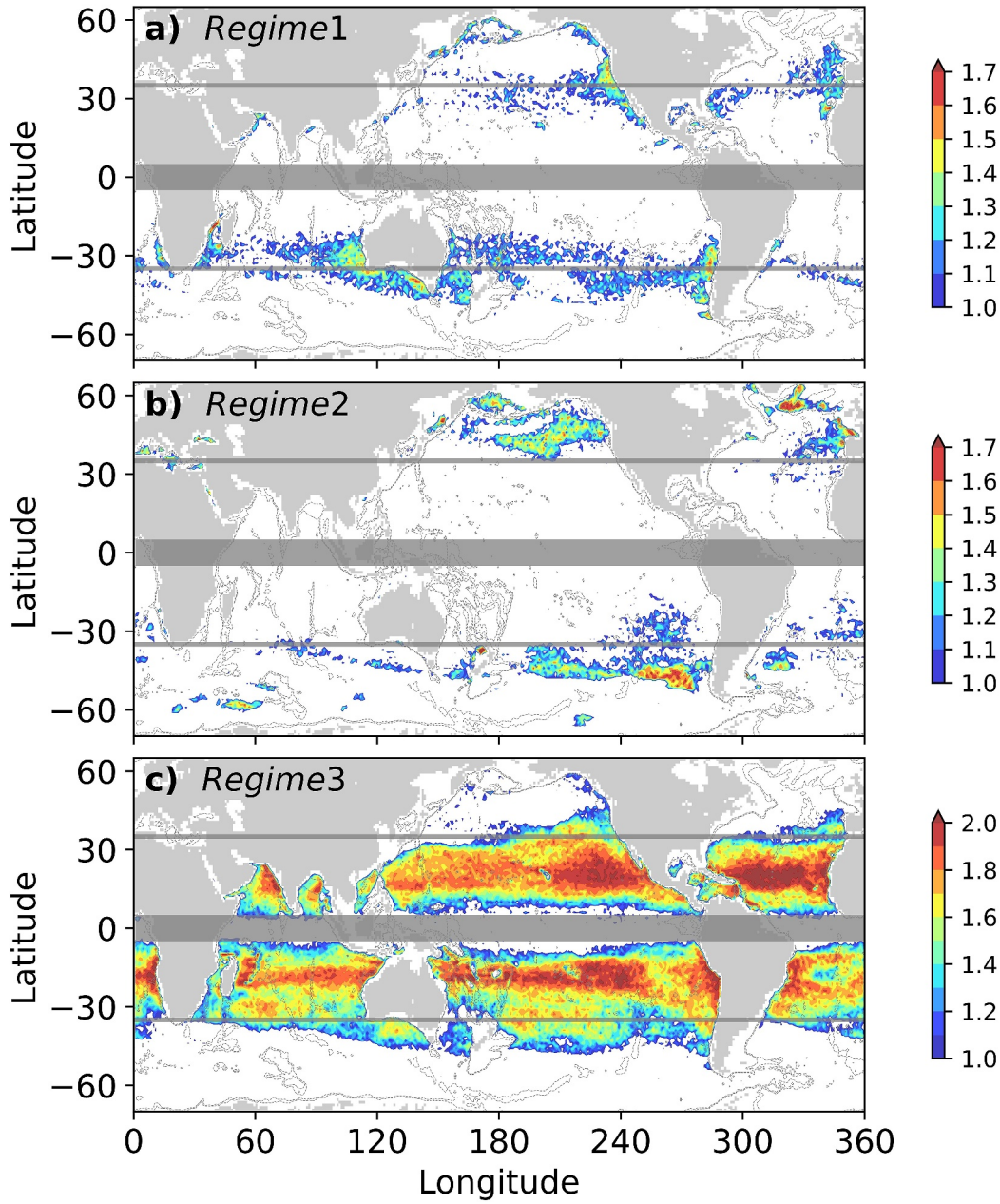

Figure 4. Global distributions of eddies falling into Regimes 1, 2, and 3 defined in Figure 3, shown as the base-10 logarithms of eddy counts per 1° (latitude) × 2° (longitude) grid box. The 35° latitudes are highlighted by gray horizontal lines.

estimate the propagation speeds of eastward-propagating eddies with relatively strong nonlinearity, ranging between 6 and 15 (Figure 5).

With L_d adopted for theorizing eastward propagation of eddies, the fraction of eddy propagation speed records with relative errors bounded by ±25% slightly increases from 38.3% (34.0%) to 40.6% (37.4%) for anticyclonic (cyclonic) mesoscale eddies if the local eddy wavelengths are further taken into account. However, such relative errors grow if $L_{d|_{\text{surf}}}$ is adopted for quantifying the deformation scale. In this case, the fraction of eddy propagation speed records with relative errors bounded by ±25% drops to 26.8% for AE and 24.9% for CE. In general, incorporating the local eddy scale and L_d into the theoretical phase speed is equally favorable to quantifying eddy propagation poleward of 35° latitudes.

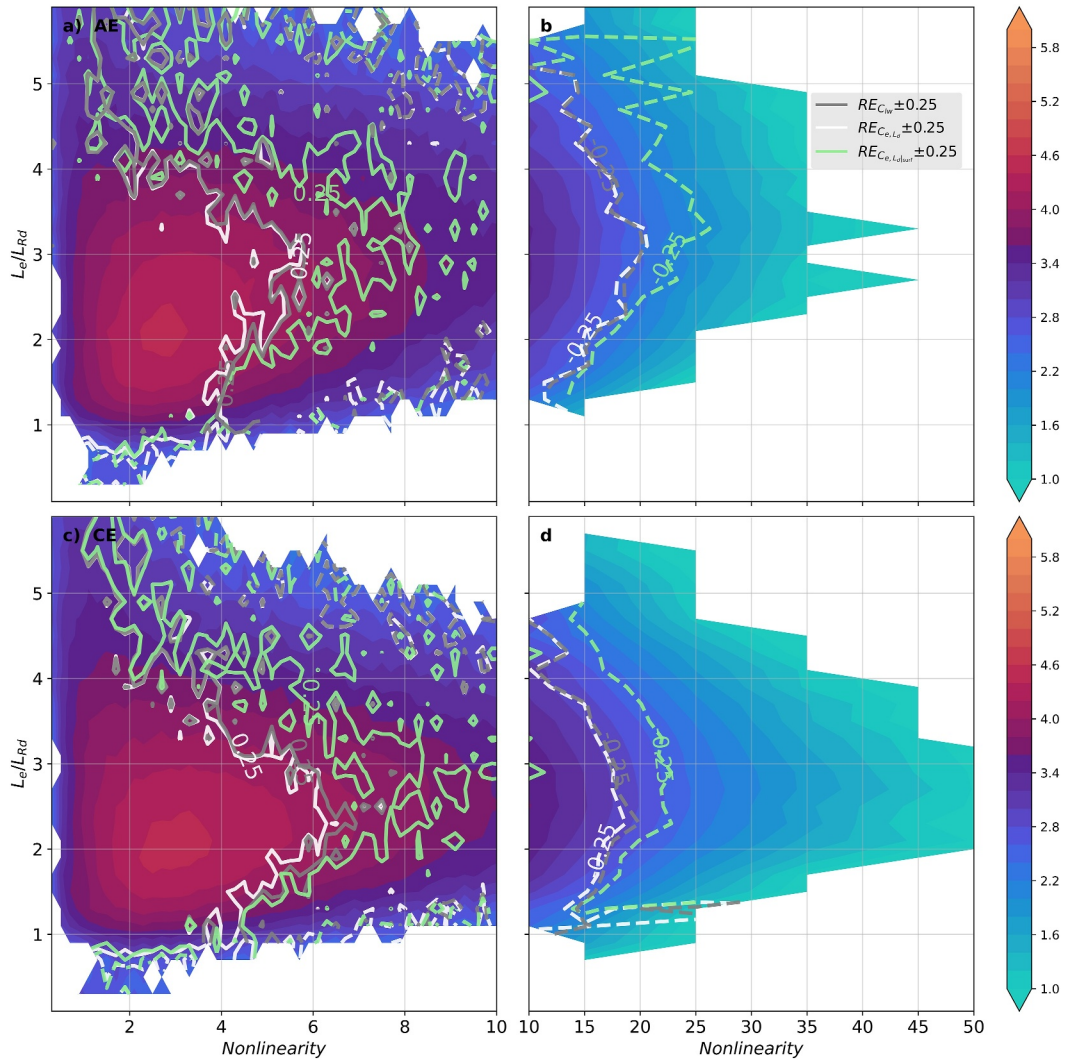

Figure 5. Similar to Figure 3 but for eastward-propagating eddies. Only theoretically estimated eddy propagation speeds with an eastward direction are considered for calculating the relative errors, which account for approximately 55% of observed eastward eddy propagation records.

4. Discussion

This study highlights the efficacy of the baroclinic Rossby wave phase speed, by incorporating the local eddy length scale, in accurately capturing the zonal propagation speed of most observed mesoscale eddies (C_{obs}) during the satellite altimetry era. Such efficacy is particularly evident in low-latitude regions, where our proposed approach significantly outperforms theoretical estimates of eddy zonal speed based on the long Rossby wave approximation. However, if the observational zonal propagation speeds of SSH anomalies inferred from the Radon transform (C_{Radon}) were treated as the ground truth, as was done by Tulloch et al. (2009), then the predictive skill of long baroclinic Rossby wave phase speeds is adequate within 20° of latitudes from equator but increasingly deteriorates toward higher latitudes (Figures 1a and 1b), consistent with previous findings (Chelton et al., 2007; Chelton & Schlax, 1996; Tulloch et al., 2009). Moreover, C_{Radon} in the extratropics cannot be accurately framed by solutions of the linear QG system, even if a finite wavelength was optimally fitted by Tulloch et al. (2009). This discrepancy highlights the fundamental difference between the observational zonal propagation speeds obtained through mesoscale SSH anomaly tracking algorithms and those derived from the Radon transform of SSH Hovmöller diagrams (Chelton et al., 2011).

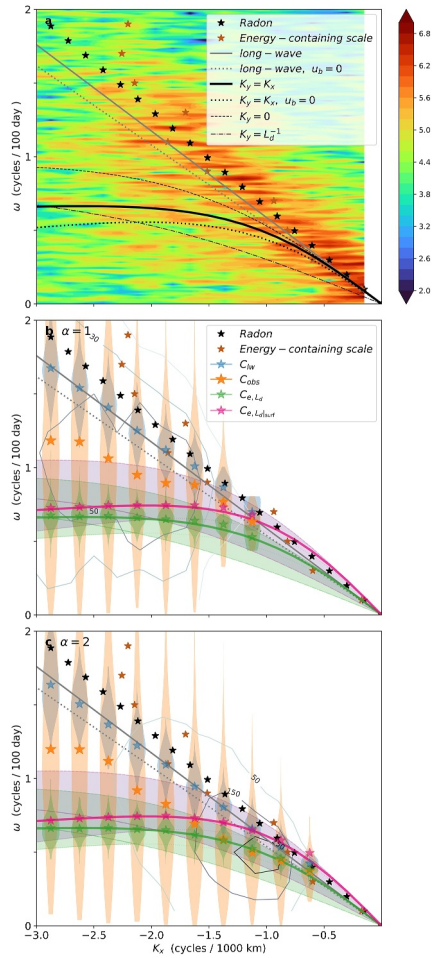

Figure 6. (a) Color shading shows the zonal wavenumber and frequency spectrum of sea surface height (SSH) anomaly. Black pentagrams represent the wave dispersion relation calculated from observed zonal propagation speeds of SSH anomalies, derived from Radon transform. Brown pentagrams denote the energy-containing scales, estimated at each frequency via the wavenumber centroid of SSH anomaly spectrum. The black solid curve indicates the Rossby wave dispersion relation constructed by assuming horizontal isotropy and by accounting for the Doppler-shift effect from the depth-mean background velocity of −0.006 m/s. The black dotted curve is similar to the black solid curve but constructed by excluding the Doppler-shift effect. The black dashed and black dashed-dotted curves are similar to the black solid curve but constructed by assuming vanishing meridional wavenumber and deformation meridional scale, respectively. The gray solid curve indicates the dispersion relation of long baroclinic Rossby waves, Doppler-shifted by the depth-mean zonal velocity. The gray dotted curve is similar to the gray solid curve but constructed by excluding the Doppler-shift effect. (b) With $\alpha = 1$, the background contours indicate total eddy counting levels of 10, 30, and 50 within 24 ° ± 0.5°N latitudinally in spectral space constructed with frequency bins of 0.2 cycles/(100 days) and zonal wavenumber bins of 0.02 cycles/(1000 km). Orange violins indicate the distribution of observed mesoscale eddy frequency, $\frac{2\pi}{(\alpha L_e)} C_{\text{obs}}$, calculated in each zonal wavenumber bin of 0.25 cycles/(1000 km). Green (Magenta) and blue violins indicate distributions of estimated mesoscale eddy frequencies, $\frac{2\pi}{(\alpha L_e)} C_{e,L_d}$ $\left(\frac{2\pi}{(\alpha L_e)} C_{e,L_{d|\text{surf}}}\right)$ based on the proposed theoretical eddy propagation speed (Equations 6 and 7) in this study and $\frac{2\pi}{(\alpha L_e)} C_{lw}$ based on the long-wave approximation, respectively. Pentagrams indicate the mean values of corresponding eddy frequency variants. The green and magenta curves show the theoretical eddy frequencies $K_x C_{e,L_d}$ and $K_x C_{e,L_{d|\text{surf}}}$, respectively, with shaded areas indicating the ranges of these theoretical estimates under varying conditions of eddy anisotropy, consistent with the diagnostics shown in panel (a). (c) Same as panel (b) but with $\alpha = 2$; the background contours now indicate total eddy counting levels of 50, 150, and 250.

To further see the source of this fundamental difference, we construct in Figure 6a the zonal wavenumber-frequency spectrum of SSH anomalies along the latitudinal band of 24°N, between 170°W and 125°E, following Early et al. (2011) and Lacasce (2017), but with the extended 30-year-long altimetry record (for coherent eddy counting and statistics, the region spans 24° ± 0.5°N latitudinally). In addition, we superpose multiple dispersion curves of baroclinic Rossby wave phase speeds, calculated with or without the Doppler-shift effect from the background westward speed of approximately 6×10^{-3} m/s in the selected region. As in previous studies (Early et al., 2011; Lacasce, 2017), SSH anomaly variance is visibly pronounced along the dispersion curves of long baroclinic Rossby waves (gray curves), particularly toward larger wavenumbers, but is weakened around the finite-wavenumber dispersion relations with lower frequencies. Not surprisingly but importantly, the dispersion curve calculated with the averaged C_{Radon} (black pentagrams) in this region is also closely aligned with energy-containing SSH signatures (brown pentagrams), the latter of which is identified via the wavenumber centroid of SSH spectrum for each selected frequency. This is consistent with the previous notion that the Radon transform acts as a low-pass filter (Chelton et al., 2011; Klocker & Marshall, 2014) and may therefore favor the most energetic SSH features resulting from an inverse turbulent energy cascade (Kong & Jansen, 2017). However, the total eddy count distribution in wavenumber-frequency spectral space indicates that most eddies, particularly those of smaller spatial scales, tend to propagate at baroclinic Rossby wave phase speeds with finite wavenumbers, rather than at long-wave phase speeds (see solid contours of eddy count in Figures 6b and 6c). This observation holds true regardless of whether α remains at unity or gets doubled. Quantitatively, only about 12% of the total eddy population in the selected region are associated with the energy-containing scale (as identified from the eddy counts within the same spectral bins of energy-containing wavenumbers). Overall, the long-wave approximation appears as an upper bound of ocean eddy propagation speeds, primarily characterizing the most energetic but less abundant eddies. Consequently, the dispersion curve inferred from the Radon transform of SSH primarily captures the "long-wave portion" of the eddy population depicted in the spectral heatmap.

The discrepancy of propagation speeds of less energetic but more abundant eddies against those of energy-containing eddies toward low latitudes has implications for parameterizing eddy mixing, whose efficiency was found to depend crucially on the intrinsic eddy propagation (Ferrari & Nikurashin, 2010; Klocker & Abernathey, 2014). On the one hand, our reported discrepancy is consistent with recent observations based on the global eddy census (Chelton et al., 2011) that faster-propagating and more energetic eddies generally possess shorter lifecycles (Liu et al., 2022), which may lessen the contribution to eddy mixing globally. By contrast, eddies characterized by lower energy and slower propagation may adequately smear the large-scale tracer gradients in a long run. On the other hand, energy-containing eddies with propagation speeds aligned closely with the

theoretical long-wave speeds have been argued to be wave- or jet-like toward low latitudes (Kong & Jansen, 2017) and hence less effective in driving irreversible mixing (Klocker & Abernathey, 2014). This finds evidence in Klocker and Abernathey (2014), who observed that long-wave phase speeds substantially exceeded the eddy propagation speeds inferred from the actual eddy diffusivity in tropical regions. These hypotheses regarding eddy-driven mixing are pertinent to our observations and merit further in-depth investigation in future work.

The remaining discrepancies between the revised theoretical propagation speeds and the observations likely stem from three sources of uncertainties: (a) the background zonal velocity, (b) the estimates of deformation radii, and (c) the estimates of local eddy length scales. We hereby discuss these uncertainties successively.

First, the background zonal flow used in this study is based on monthly data with a spatial resolution of 1°, whereas the observed eddy propagation speeds are derived from daily altimetry data at a 1/4° resolution. Such mismatches in temporal and spatial resolutions can compromise a source of theory-observation deviation. Moreover, selecting the seafloor as the no-flow vertical level in exploiting the thermal wind balance is a simple approximation, which may not be always valid.

Second, the choice of the deformation radius directly influences the discrepancy between theoretical and observed propagation speeds. That is, the vertical modal structure associated with an eddy affects its zonal propagation speed. Based on our observations, eddies near the eastern boundaries are more accurately characterized using the traditional first-mode deformation radius (L_d), whereas eddies in the mid-latitude open ocean are more appropriately represented by the surface-mode deformation radius ($L_{d|_{\mathrm{surf}}}$).

Third, the local eddy length scale in this study is estimated using the eddy radius, which is defined as the radius of a circle with an identical area to that of the SSH contour associated with the maximized circum-average geostrophic speed of an eddy. This definition may underestimate the true eddy length scale, particularly in low-latitude regions. This can be seen in Figure 6b, where a significant mismatch of the dispersion relationship between the observations (orange pentagrams) and the theories, including those using L_d (green pentagrams) and $L_{d|_{\mathrm{surf}}}$ (magenta pentagrams) in the dominant spatial scales of mesoscale eddies (approximately 3 to 1.5 cycles/1000 km).

However, when an empirical correction factor of $\alpha = 2$ is adopted, the aforementioned spectral mismatch is mitigated (Figure 6c), suggesting that the actual eddy wavelength may be approximately eight times the eddy radius in this region. With this correction, the theoretical dispersion relation using L_d shows a significantly improved match with the observed dispersion relation of most eddies, whose scales are generally smaller than 1.5 cycles/1000 km. In contrast, theoretical speeds based on $L_{d|_{\mathrm{surf}}}$ tend to overestimate the observed propagation speeds of these smaller-scale eddies.

In general, accurately and efficiently estimating the local eddy scale is essential for predicting their propagation speeds, especially in the mid- to low-latitudes. To pragmatically address the systematic bias between the nominal eddy radius and the actual eddy wavelength, we introduce an empirical correction factor α. We find that a selection of $\alpha = 2$ brings the L_d-based revised theoretical phase speed to a more universal agreement with the observed average zonal propagation speeds for both AE and CE in low- to mid-latitude regions (see Figure 7, which reconstructs the comparisons between theoretical and observational eddy propagation speeds but with different α values). More quantitatively, the ratio between the observational eddy speeds and the L_d-based theoretical speeds with $\alpha = 2$ is much closer to unity across 10°–35° latitudes (Figures 7b and 7d).

5. Conclusions

Mesoscale eddies are prevalent throughout the global ocean and exhibit a distinct westward translational tendency, which constitutes a key feature of oceanic geostrophic turbulence (Cushman-Roisin et al., 1990; Killworth, 1986; McWilliams & Flierl, 1979). Previous studies have indicated that the zonal propagation speeds of these eddies can be predicted using the long baroclinic Rossby wave phase speeds, adjusted with the Doppler-shift effect from the depth-mean zonal flow (Klocker & Marshall, 2014; LaCasce & Groeskamp, 2020). However, the accuracy of these predictions diminishes significantly equatorward of approximately ∼35° latitudes (Chelton et al., 2007), introducing substantial overestimation biases for mesoscale eddy diffusivity (Klocker & Abernathey, 2014).

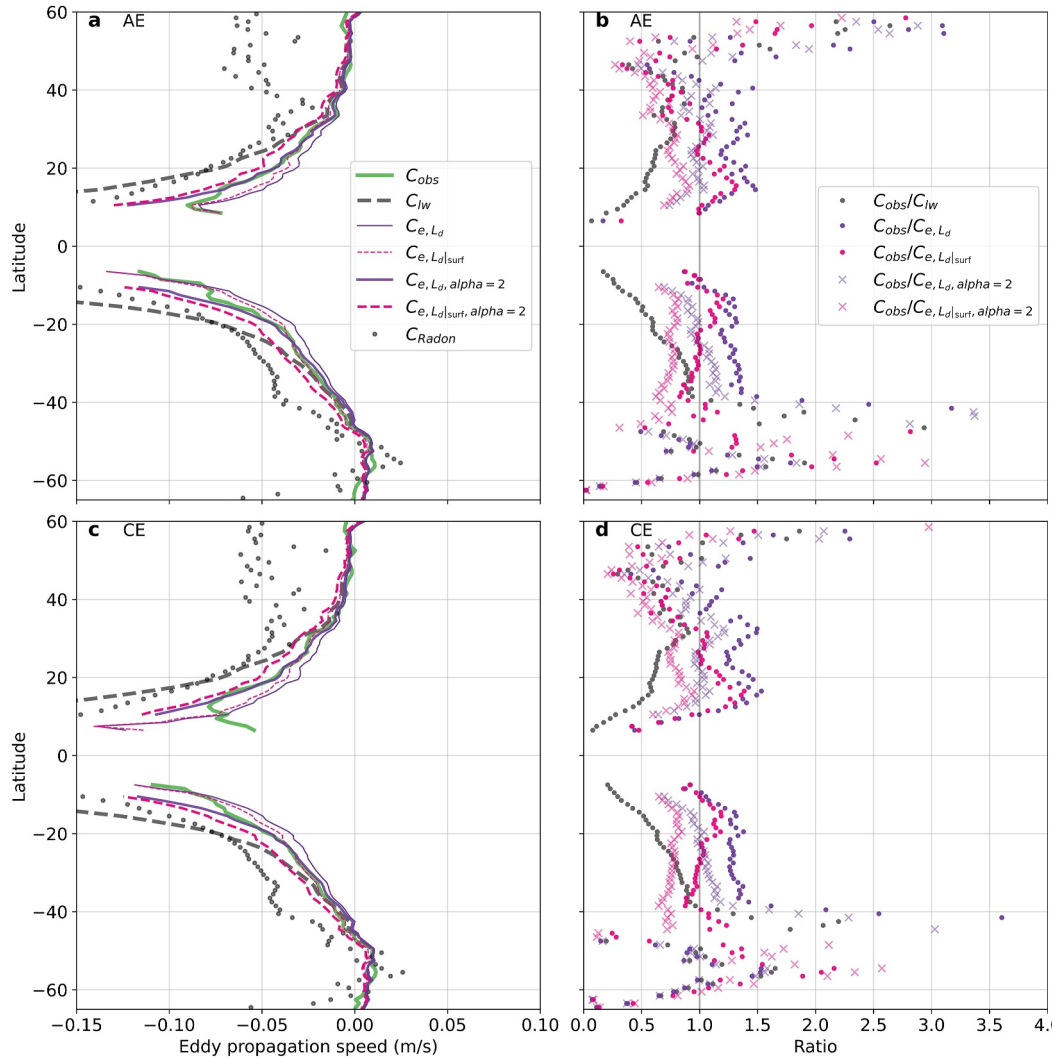

Figure 7. (a) Similar to Figure 1a, but including revised theoretical estimates using $\alpha = 2$ for anticyclonic eddies. (b) Black dots indicate the ratio between observed eddy propagation speeds and those predicted by the long-wave theoretical approximation. Purple and magenta dots (crosses) show the ratios between observed propagation speeds and revised theoretical estimates constructed using L_d and $L_{d|_{surf}}$, respectively, with $\alpha = 1$ ($\alpha = 2$). (c) Similar to panel (a) but for cyclonic eddies (CE). (d) Similar to panel (b) but for CE.

This study remedies this issue by incorporating the local eddy length scale into the baroclinic Rossby wave speed, which is shown to substantially alleviate the overestimation across the low latitudes and enables a more accurate quantification of the zonal propagation of mesoscale eddies in the satellite altimetry era. The improvement of this theoretical estimation is attributed to the observations that many mesoscale eddies have length scales comparable to the deformation scales and exhibit moderate nonlinearity in the mid-to low-latitudes. These findings further indicate that mesoscale eddy propagation is ubiquitously dispersive. Meanwhile, the revised theoretical estimation readily converges toward that based on the long-wave approximation if the eddy length scales are adequately large compared to the local deformation radii, such as those in the Southern Ocean, but remains to be slightly more accurate than the long-wave-based prediction.

In revising the theoretical estimation of eddy speeds, we find that the eddy radius, defined conventionally by the circle with an area equal to that enclosed by the SSH contour supporting the maximized circum-average eddy speed, can be a useful and convenient metric of the local eddy length scale. Importantly, this length scale does not always resemble the energy-containing scale of geostrophic turbulence, but rather characterizes most coherent eddies observed via satellite altimetry.

The phase speeds of linear PV waves with deformation length scales generally align with the revised theoretical Rossby wave phase speeds equatorward of approximately ∼20°, but tend to delineate a lower bound for the westward eddy propagation toward higher latitudes. This seems to echo with previous findings that low-latitude transient features are dominated by linear waves and that eddies turn increasingly nonlinear away from equator. However, our analyses of available observations reveal that, even with high nonlinearity, abundant extratropical coherent eddies propagate at speeds consistent with those of baroclinic Rossby waves.

This study underscores the importance of accurately estimating the background zonal flow, deformation radii, and local eddy length scales in achieving higher accuracy in theoretical estimates of eddy propagation speeds. First, more precise measurements of the no-flow level or the bottom flow velocity, particularly in regions with intense jet flows such as the Southern Ocean, would substantially facilitate the quantification of the Doppler-shift effect on eddy propagation. Second, mesoscale eddies across different oceanic regions may exhibit distinct vertical modal structures; this requires the use of regionally dependent deformation radius variants to better capture eddy propagation dynamics. Third, the actual spatial scale of an eddy may differ from its geometric radius defined by the maximum circum-average geostrophic speed. With an empirical correction factor of $\alpha = 2$, the L_d-based revised theoretical phase speeds exhibit a universal agreement with the observed zonal propagation speeds on a global scale. This correction thus serves as a practical starting point for accurately predicting the length scales and thus the zonal propagation of mesoscale eddies in future work.

Lastly, the findings and data set from this work are anticipated to contribute to understanding the long-range propagating behaviors of mesoscale turbulence, which will in turn benefit studies aiming at predicting non-local mesoscale eddy effects and parameterizing eddy-driving mixing in predictive ocean climate models.

Data Availability Statement

All calculation and figure generation codes used in this study are available from Liu (2025). Observational eddy propagation speeds derived from the Radon transform are provided by C. W. Hughes and can also be accessed from Liu (2025). The surface mode deformation radius data, provided by Lacasce and Groeskamp, can be retrieved from Liu (2025). The altimetric Mesoscale Eddy Trajectories Atlas (META3.2 DT) was produced by SSALTO/DUACS and distributed by AVISO+ (https://aviso.altimetry.fr) with support from CNES, in collaboration with IMEDEA (https://doi.org/10.24400/527896/a01-2022.005). YYMMDD for the used META3.2 DT allsat version. The EN.4.2.2.c14 data (Cheng et al., 2014; Good et al., 2013) were obtained from https://www.metoffice.gov.uk/hadobs/en4/ and are C; British Crown Copyright, Met Office, provided under a Non-Commercial Government Licence (http://www.nationalarchives.gov.uk/doc/non-commercial-government-licence/version/2/).

Acknowledgments

We extend our gratitude to Joseph H. LaCasce for his constructive comments on an earlier version of this manuscript, and to Sjoerd Groeskamp for providing the global surface mode deformation radius data set. We also thank Chris W. Hughes for sharing the data set of global SSH anomaly zonal propagation speeds derived from the Radon transform. This work is supported by the Research Grants Council (RGC) of Hong Kong under the award General Research Fund 16305321, and by the Center for Ocean Research (CORE), a joint research center between Laoshan Laboratory and HKUST. Xiaoming Zhai and Julian Mak acknowledge financial support from the Royal Society Kan Tong Po International Fellowship KTP/R1/231008.

References

Abernathey, R., & Haller, G. (2018). Transport by Lagrangian vortices in the eastern Pacific. *Journal of Physical Oceanography*, *48*(3), 667–685. https://doi.org/10.1175/jpo-d-17-0102.1

Abernathey, R., & Wortham, C. (2015). Phase speed cross spectra of eddy heat fluxes in the eastern Pacific. *Journal of Physical Oceanography*, *45*(5), 1285–1301. https://doi.org/10.1175/jpo-d-14-0160.1

Aoki, K., Kubokawa, A., Sasaki, H., & Sasai, Y. (2009). Midlatitude baroclinic Rossby waves in a high-resolution OGCM simulation. *Journal of physical oceanography*, *39*(9), 2264–2279. https://doi.org/10.1175/2009jpo4137.1

Atkins, J., Andrews, O., & Frenger, I. (2022). Quantifying the contribution of ocean mesoscale eddies to low oxygen extreme events. *Geophysical Research Letters*, *49*(15), e2022GL098672. https://doi.org/10.1029/2022gl098672

Balwada, D., Xie, J.-H., Marino, R., & Feraco, F. (2022). Direct observational evidence of an oceanic dual kinetic energy cascade and its seasonality. *Science Advances*, *8*(41), eabq2566. https://doi.org/10.1126/sciadv.abq2566

Berloff, P., & Kamenkovich, I. (2013a). On spectral analysis of mesoscale eddies. Part II: Nonlinear analysis. *Journal of Physical Oceanography*, *43*(12), 2528–2544. https://doi.org/10.1175/JPO-D-12-0233.1

Berloff, P., & Kamenkovich, I. (2013b). On spectral analysis of mesoscale eddies. Part I: Linear analysis. *Journal of Physical Oceanography*, *43*(12), 2505–2527. https://doi.org/10.1175/JPO-D-12-0232.1

Bian, C., Jing, Z., Wang, H., Wu, L., Chen, Z., Gan, B., & Yang, H. (2023). Oceanic mesoscale eddies as crucial drivers of global marine heatwaves. *Nature Communications*, *14*(1), 2970. https://doi.org/10.1038/s41467-023-38811-z

Busecke, J. J., & Abernathey, R. P. (2019). Ocean mesoscale mixing linked to climate variability. *Science Advances*, *5*(1), eaav5014. https://doi.org/10.1126/sciadv.aav5014

Capet, X., Mcwilliams, J. C., Molemaker, M. J., & Shchepetkin, A. F. (2008). Mesoscale to submesoscale transition in the California current system. Part I: Flow structure, eddy flux, and observational tests. *Journal of physical oceanography*, *38*(1), 29–43. https://doi.org/10.1175/2007jpo3671.1

Chelton, D. B., DeSzoeke, R. A., Schlax, M. G., El Naggar, K., & Siwertz, N. (1998). Geographical variability of the first baroclinic Rossby radius of deformation. *Journal of Physical Oceanography*, *28*(3), 433–460. https://doi.org/10.1175/1520-0485(1998)028<0433:gvotfb>2.0.co;2

Chelton, D. B., & Schlax, M. G. (1996). Global observations of oceanic Rossby waves. *Science*, *272*(5259), 234–238. https://doi.org/10.1126/science.272.5259.234

Chelton, D. B., Schlax, M. G., & Samelson, R. M. (2011). Global observations of nonlinear mesoscale eddies. *Progress in oceanography*, *91*(2), 167–216. https://doi.org/10.1016/j.pocean.2011.01.002

Chelton, D. B., Schlax, M. G., Samelson, R. M., & de Szoeke, R. A. (2007). Global observations of large oceanic eddies. *Geophysical Research Letters*, *34*(15), L15606. https://doi.org/10.1029/2007gl030812

Chen, R., & Waterman, S. (2017). Mixing nonlocality and mixing anisotropy in an idealized western boundary current jet. *Journal of Physical Oceanography*, *47*(12), 3015–3036. https://doi.org/10.1175/jpo-d-17-0011.1

Cheng, L., Zhu, J., Cowley, R., Boyer, T., & Wijffels, S. (2014). Time, probe type, and temperature variable bias corrections to historical expendable bathythermograph observations. *Journal of Atmospheric and Oceanic Technology*, *31*(8), 1793–1825. https://doi.org/10.1175/jtech-d-13-00197.1

Cushman-Roisin, B., Tang, B., & Chassignet, E. P. (1990). Westward motion of mesoscale eddies. *Journal of Physical Oceanography*, *20*(5), 758–768. https://doi.org/10.1175/1520-0485(1990)020<0758:wmome>2.0.co;2

Early, J. J., Samelson, R., & Chelton, D. B. (2011). The evolution and propagation of quasigeostrophic ocean eddies. *Journal of Physical Oceanography*, *41*(8), 1535–1555. https://doi.org/10.1175/2011jpo4601.1

Ferrari, R., & Nikurashin, M. (2010). Suppression of eddy diffusivity across jets in the Southern Ocean. *Journal of Physical Oceanography*, *40*(7), 1501–1519. https://doi.org/10.1175/2010jpo4278.1

Garcia, H., Boyer, T., Baranova, O., Locarnini, R., Mishonov, A., Grodsky, A. e., et al. (2019). World ocean atlas 2018: Product documentation. In A. Mishonov (Ed.), *Technical editor*.

Good, S. A., Martin, M. J., & Rayner, N. A. (2013). EN4: Quality controlled ocean temperature and salinity profiles and monthly objective analyses with uncertainty estimates. *Journal of Geophysical Research: Oceans*, *118*(12), 6704–6716. https://doi.org/10.1002/2013jc009067

Groeskamp, S., LaCasce, J. H., McDougall, T. J., & Rogé, M. (2020). Full-depth global estimates of ocean mesoscale eddy mixing from observations and theory. *Geophysical Research Letters*, *47*(18), e2020GL089425. https://doi.org/10.1029/2020gl089425

He, Q., Zhan, W., Cai, S., Du, Y., Chen, Z., Tang, S., & Zhan, H. (2023). Enhancing impacts of mesoscale eddies on Southern Ocean temperature variability and extremes. *Proceedings of the National Academy of Sciences*, *120*(39), e2302292120. https://doi.org/10.1073/pnas.2302292120

Killworth, P. D. (1986). On the propagation of isolated multilayer and continuously stratified eddies. *Journal of physical oceanography*, *16*(4), 709–716. https://doi.org/10.1175/1520-0485(1986)016<0709:otpoim>2.0.co;2

Klocker, A., & Abernathey, R. (2014). Global patterns of mesoscale eddy properties and diffusivities. *Journal of Physical Oceanography*, *44*(3), 1030–1046. https://doi.org/10.1175/jpo-d-13-0159.1

Klocker, A., Ferrari, R., LaCasce, J. H., & Merrifield, S. T. (2012). Reconciling float-based and tracer-based estimates of lateral diffusivities. *Journal of Marine Research*, *70*(4), 569–602. https://doi.org/10.1357/002224012805262743

Klocker, A., & Marshall, D. P. (2014). Advection of baroclinic eddies by depth mean flow. *Geophysical Research Letters*, *41*(10), 3517–3521. https://doi.org/10.1002/2014gl060001

Klocker, A., Marshall, D. P., Keating, S. R., & Read, P. L. (2016). A regime diagram for ocean geostrophic turbulence. *Quarterly Journal of the Royal Meteorological Society*, *142*(699), 2411–2417. https://doi.org/10.1002/qj.2833

Kong, H., & Jansen, M. F. (2017). The eddy diffusivity in barotropic β-plane turbulence. *Fluid*, *2*(4), 54. https://doi.org/10.3390/fluids2040054

Lacasce, J. H. (2017). The prevalence of oceanic surface modes. *Geophysical Research Letters*, *44*(21), 11–97. https://doi.org/10.1002/2017gl075430

LaCasce, J. H., & Groeskamp, S. (2020). Baroclinic modes over rough bathymetry and the surface deformation radius. *Journal of Physical Oceanography*, *50*(10), 2835–2847. https://doi.org/10.1175/jpo-d-20-0055.1

Liu, R. (2025). Improved theoretical estimates of the zonal propagation of global nonlinear mesoscale eddies. *Zenodo*. https://doi.org/10.5281/zenodo.14849009

Liu, R., Wang, G., & Balwada, D. (2024). The multi-scale response of the eddy kinetic energy and transport to strengthened westerlies in an idealized Antarctic circumpolar current. *Authorea Preprints*, *51*(8). https://doi.org/10.1029/2023gl106747

Liu, R., Wang, G., Chapman, C., & Chen, C. (2022). The attenuation effect of jet filament on the eastward mesoscale eddy lifetime in the Southern Ocean. *Journal of Physical Oceanography*, *52*(5), 805–822. https://doi.org/10.1175/jpo-d-21-0030.1

McDougall, T. J., & Barker, P. M. (2011). Getting started with teos-10 and the Gibbs seawater (GSW) oceanographic toolbox. *Scor/iapso WG*, *127*(532), 1–28.

McGillicuddy, D. J., Jr. (2016). Mechanisms of physical-biological-biogeochemical interaction at the oceanic mesoscale. *Annual Review of Marine Science*, *8*(1), 125–159. https://doi.org/10.1146/annurev-marine-010814-015606

McWilliams, J. C. (2008). The nature and consequences of oceanic eddies. *Geophysical monograph series*, *177*, 5–15. https://doi.org/10.1029/177gm03

McWilliams, J. C., & Flierl, G. R. (1979). On the evolution of isolated, nonlinear vortices. *Journal of Physical Oceanography*, *9*(6), 1155–1182. https://doi.org/10.1175/1520-0485(1979)009<1155:oteoin>2.0.co;2

Pegliasco, C., Delepoulle, A., Mason, E., Morrow, R., Faugère, Y., & Dibarboure, G. (2022). META3. 1exp: A new global mesoscale eddy trajectory atlas derived from altimetry. *Earth System Science Data*, *14*(3), 1087–1107. https://doi.org/10.5194/essd-14-1087-2022

Salmon, R. (1982). Geostrophic turbulence. *Topics in ocean physics*, *30*, 78.

Scott, R. B., & Wang, F. (2005). Direct evidence of an oceanic inverse kinetic energy cascade from satellite altimetry. *Journal of Physical Oceanography*, *35*(9), 1650–1666. https://doi.org/10.1175/jpo2771.1

Smith, K. S. (2007). The geography of linear baroclinic instability in earth's oceans. *Journal of Marine Research*, *65*(5), 655–683. https://doi.org/10.1357/002224007783649484

Stewart, K., Spence, P., Waterman, S., Le Sommer, J., Molines, J.-M., Lilly, J., & England, M. H. (2015). Anisotropy of eddy variability in the global ocean. *Ocean Modelling*, *95*, 53–65. https://doi.org/10.1016/j.ocemod.2015.09.005

Tailleux, R. (2012). On the generalized eigenvalue problem for the Rossby wave vertical velocity in the presence of mean flow and topography. *Journal of physical oceanography*, *42*(6), 1045–1050. https://doi.org/10.1175/jpo-d-12-010.1

Tailleux, R., & McWilliams, J. C. (2000). Acceleration, creation, and depletion of wind-driven, baroclinic Rossby waves over an ocean ridge. *Journal of physical oceanography*, *30*(9), 2186–2213. https://doi.org/10.1175/1520-0485(2000)030<2186:acadow>2.0.co;2

Tailleux, R., & McWilliams, J. C. (2001). The effect of bottom pressure decoupling on the speed of extratropical, baroclinic Rossby waves. *Journal of physical oceanography*, *31*(6), 1461–1476. https://doi.org/10.1175/1520-0485(2001)031<1461:teobpd>2.0.co;2

Tulloch, R., Marshall, J., Hill, C., & Smith, K. S. (2011). Scales, growth rates, and spectral fluxes of baroclinic instability in the ocean. *Journal of Physical Oceanography*, *41*(6), 1057–1076. https://doi.org/10.1175/2011jpo4404.1

Tulloch, R., Marshall, J., & Smith, K. S. (2009). Interpretation of the propagation of surface altimetric observations in terms of planetary waves and geostrophic turbulence. *Journal of Geophysical Research*, *114*(C2), C02005. https://doi.org/10.1029/2008jc005055

Uchida, T., Balwada, D., Abernathey, R. P., McKinley, G. A., Smith, S. K., & Lévy, M. (2020). Vertical eddy iron fluxes support primary production in the open southern ocean. *Nature Communications*, *11*(1), 1125. https://doi.org/10.1038/s41467-020-14955-0

Vallis, G. K. (2017). *Atmospheric and oceanic fluid dynamics*. Cambridge University Press.

Wang, H., Qiu, B., Liu, H., & Zhang, Z. (2023). Doubling of surface oceanic meridional heat transport by non-symmetry of mesoscale eddies. *Nature Communications*, *14*(1), 5460. https://doi.org/10.1038/s41467-023-41294-7

Wortham, C., & Wunsch, C. (2014). A multidimensional spectral description of ocean variability. *Journal of physical oceanography*, *44*(3), 944–966. https://doi.org/10.1175/jpo-d-13-0113.1

Wunsch, C., & Stammer, D. (1995). The global frequency-wavenumber spectrum of oceanic variability estimated from topex/poseidon altimetric measurements. *Journal of Geophysical Research*, *100*(C12), 24895–24910. https://doi.org/10.1029/95jc01783

Xu, F.-H., & Oey, L.-Y. (2015). Seasonal SSH variability of the northern South China Sea. *Journal of Physical Oceanography*, *45*(6), 1595–1609. https://doi.org/10.1175/jpo-d-14-0193.1

Youngs, M. K., Freilich, M. A., & Lovenduski, N. S. (2023). Air-Sea CO_2 fluxes localized by topography in a Southern Ocean channel. *Geophysical Research Letters*, *50*(18), e2023GL104802. https://doi.org/10.1029/2023gl104802

Zhang, W., & Wolfe, C. L. (2024). Inferring tracer diffusivity from coherent mesoscale eddies. *Journal of Advances in Modeling Earth Systems*, *16*(4), e2023MS004004. https://doi.org/10.1029/2023ms004004

Zhang, Z., & Qiu, B. (2018). Evolution of submesoscale ageostrophic motions through the life cycle of oceanic mesoscale eddies. *Geophysical Research Letters*, *45*(21), 11–847. https://doi.org/10.1029/2018gl080399